Advances in Radiation Oncology (2021) 6, 100716

advances in radiation oncology

www.advancesradonc.org

Scientific Article

Tumor Treating Fields for Ovarian Carcinoma: A Modeling Study

Edwin Lok, MS,[a,b,*] Pyay San, BS,[a] Victoria White, BS,[a] Olivia Liang, BS,[a] Page C. Widick, MD,[c] Sindhu Pisati Reddy, MD,[a] and Eric T. Wong, MD[a,**]

[a]*Brain Tumor Center & Neuro-Oncology Unit, Beth Israel Deaconess Medical Center, Boston, Massachusetts;*
[b]*Department of Radiation Oncology, US Oncology/Signature Healthcare of Brockton, Brockton, Massachusetts;*
[c]*Division of Hematology/Oncology, Department of Medicine, Beth Israel Deaconess Medical Center, Boston, Massachusetts*

Received December 8, 2020; revised March 10, 2021; accepted April 14, 2021

Abstract

Purpose: Since the inception of tumor treating fields (TTFields) therapy as a Food and Drug Administration–approved treatment with known clinical efficacy against recurrent and newly diagnosed glioblastoma, various in silico modeling studies have been performed in an effort to better understand the distribution of applied electric fields throughout the human body for various malignancies or metastases.

Methods and Materials: Postacquisition attenuation-corrected positron emission tomography–computed tomography image data sets from 2 patients with ovarian carcinoma were used to fully segment various intrapelvic and intra-abdominal gross anatomic structures. A 3-dimensional finite element mesh model was generated and then solved for the distribution of applied electric fields, rate of energy deposition, and current density at the clinical target volumes (CTVs) and other intrapelvic and intra-abdominal structures. Electric field-volume histograms, specific absorption rate–volume histograms, and current density-volume histograms were generated, by which plan quality metrics were derived from and used to evaluate relative differences in field coverage between models under various conditions.

Results: TTFields therapy distribution throughout the pelvis and abdomen was largely heterogeneous, where specifically the field intensity at the CTV was heavily influenced by surrounding anatomic structures as well as its shape and location. The electric conductivity of the CTV had a direct effect on the field strength within itself, as did the position of the arrays on the surface of the pelvis and/or abdomen.

Conclusion: The combined use of electric field-volume histograms, specific absorption rate-volume histograms, current density-volume histograms, and plan quality metrics enables a personalized method to dosimetrically evaluate patients receiving TTFields therapy for ovarian carcinoma when certain patient- and tumor-specific factors are integrated with the treatment plan.

Sources of support: This research was supported in part by *A Reason To Ride* research fund and The Musella Foundation.

Disclosures: E.T.W. received grants from Novocure during the conduct of the study, grants from AstraZeneca, grants from Five Prime Therapeutics, grants from Immunocellular Therapeutics, grants from Merck, grants from Pfizer, grants from Plexxicon, grants from Vascular Biogenics, and personal fees and other from ZaiLab, outside the submitted work.

Research data are available at doi:10.7303/syn23623067.

S.P.R.'s current address: Department of Neurology, Southern Illinois University School of Medicine.

*Corresponding author: Edwin Lok, MS; E-mail: elok@bidmc.harvard.edu.

**Corresponding author: Eric T. Wong, MD; E-mail: ewong@bidmc.harvard.edu.

https://doi.org/10.1016/j.adro.2021.100716

Introduction

Ovarian carcinoma is a heterogeneous disease with various histologic types[11]. Combination chemotherapy with carboplatin and paclitaxel, with or without bevacizumab, remains the standard of care in patients with advanced disease[2,15]. The addition of maintenance poly (ADP-ribose) polymerase inhibitor, either olaparib or niraparib depending on patient characteristics, also resulted in a survival benefit[5,13]. One of the difficulties in the management of disseminated ovarian cancer is its propensity of spreading to the abdominal and/or peritoneal cavicrty, creating challenges for locoregional radiation, intraperitoneal chemotherapy, and systemic drug treatments, all of which have been found ineffective for most patients[3,7,14,16,17,22,23]. Clearly, there is a need for new therapies for advanced ovarian cancer.

Tumor treating fields (TTFields) are alternating electric fields tuned to 150 to 300 kHz that have an antiproliferative effect on various tumor types. TTFields therapy at 200 kHz has been approved by the Food and Drug Administration for the treatment of newly diagnosed and recurrent glioblastomas[20,21]. This therapy offers an unequivocal survival benefit in these populations[21]. For ovarian cancer, the optimal frequency for tumor control is also at 200 kHz[4]. A phase II study combining TTFields with weekly paclitaxel for platinum-resistant ovarian carcinoma showed a partial response rate of 25%, a clinical benefit rate of 71%, and a median progression-free survival of 8.9 months, while the median overall survival was not reached[24]. Therefore, TTFields therapy may have efficacy against ovarian cancer, and it is currently being tested in a randomized phase III clinical trial (NCT03940196).

TTFields can be quantified by finite element modeling, and the dosimetry can be influenced by tissue composition, tissue geometry, target location, positioning of the arrays, proximity to conductive fluids, and attenuation from high impedance cancellous and cortical bones. For example, in glioblastoma, TTFields are influenced by the presence or absence of a conductive necrotic core, the proximity of the gross tumor volume (GTV) to neighboring cerebrospinal fluid and bilateral ventricles, the total volume of cerebrospinal fluid, and array positioning on the scalp[8,10,26,27]. However, for ovarian cancer, factors that influence field distribution within the abdomen, peritoneal cavity, and the pelvis are incompletely understood. Voloshin et al[25] performed a preliminary modeling study showing that the field distribution within the peritoneal cavity had a peak-to-peak (pk-pk) average intensity of 1.85 V/cm. They also revealed that 95% of the abdomen received field intensity greater than 1.53 V/cm pk-pk, and 60% of the field was higher than 2.55 V/cm pk-pk. However, this study did not disclose the metrics used to characterize TTFields within specific tissues or explain differences in field distribution due to array positioning. In our study, we used 2 pairs of orthogonally positioned arrays to compute the field distribution within the pelvis and abdomen. We also quantified the electric field intensity, specific absorption rate, and current density for various segmented intrapelvic and intra-abdominal structures using finite element modeling and plan quality metrics (PQM) derived from electric field (E) volume histogram, specific absorption rate (SAR) volume histogram, and current density (CD) volume histogram. In addition, we performed sensitivity analyses by altering the electric conductivity of the clinical target volume (CTV) and bladder and rotating the arrays around the abdomen and pelvis.

Methods and Materials

Two patients with ovarian cancer, transitional cell carcinoma with malignant ascites in NS001 and BRCA1-positive ovarian carcinoma in BM002, were identified. Detailed presentation and treatment histories are described in the Appendix E1. Because TTFields have emerged as a potential therapeutic modality for malignancies in the abdomen and pelvis[24], we sought to model in silico the extent and distribution of TTFields. Segmentation of the CTVs, critical intrapelvic organs, and relevant intra-abdominal structures, such as those listed in Table 1, was performed on posthysterectomy computed tomography data set from NS001 and preoperative attenuation corrected positron emission tomography-computed tomography data set from BM002, using ScanIP 2019 (Simpleware LTD, UK), where a mixture of grayscale thresholding and manual segmentation methods was used. Certain structures, such as bones, muscles, and various vessels, were merged into larger entities to maximize modeling efficiency without compromising quality. Electrodes and conductive gel layers between each electrode and skin surface were manually applied, and conductive gel layers were added to ensure uniform distribution of applied alternating electric fields. Electrode array dimensions were specified, mimicking those from the NovoTTF-100L(O) system[24], and all 4 arrays were used in our study. Upon completion of the segmentation, a 3-dimensional finite element mesh model was generated within ScanIP and then imported into COMSOL Multiphysics 5.5 (COMSOL, Burlington, MA), where material properties, boundary conditions, and required physics parameters were assigned (Table 1). The electric field distribution within the model was then solved using the AC/DC module in the frequency domain, where magnetic fields and magnetically induced currents were assumed to be negligible.

To formulate a comprehensive method of evaluating the model and quantitatively comparedifferences in

Table 1 Relevant material properties for segmented anatomical structures in the abdomen and pelvis

Tissue structure	Electric conductivity σ (S/m)	Physical density ρ (kg/m^3)
CTV (NS001)	1.30E + 00	2000
CTV_p (BM002)	2.50E-01[18,29]	1100
CTV_n (BM002)	2.50E-01[18,29]	1100
Anal canal	2.51E-01	1088
Anal sphincter	3.73E-01	1090
Bladder	1.75E + 00	1024
Bladder wall	2.20E-01	1086
Blood vessels	7.06E-01	1050
Bulb of vestibule	2.51E-01	1088
Cancellous bone	8.43E-02	1178
Cerebrospinal fluid	2.00E + 00	1007
Clitoris	2.51E-01	1088
Coccyx	2.09E-02	1908
Colon	2.51E-01	1088
Cortical bone	2.09E-02	1908
Fat	4.35E-02	911
Femur (left/right)	2.09E-02	1908
Gallbladder	9.00E-01	1071
Gas	1.00E-09	1
Ilium	2.09E-02	1908
Ischium	2.09E-02	1908
Kidney	1.88E-01	1066
Liver	1.05E-01	1079
Lumbar spine	2.09E-02	1908
Muscle	3.73E-01	1090
Pancreas	5.43E-01	1087
Pubis	2.09E-02	1908
Rectum	2.51E-01	1088
Sacrum	2.09E-02	1908
Skin	1.05E-03	1109
Small bowel	6.21E-01	1030
Spinal cord	9.25E-02	1075
Spleen	1.29E-01	1089
Stomach	5.40E-01	1088
Urethra	3.20E-01	1102
Uterus	5.38E-01	1105
Vagina	2.51E-01	1088
Electrodes	1.00E-05	11,000
Hydrogel	1.00E-01	100

Abbreviations: CTV = clinical target volume; CTV_n = CTV for lymph node metastasis in the abdominal cavity; CTV_p = CTV for primary ovarian carcinoma in the pelvic cavity.

TTFields distribution, E volume histogram, SAR volume histogram, and CD volume histogram were generated within Microsoft Excel 2016. To further assess and compare specific parameters, a set of PQM derived from the respective volume histograms was created for each model. Such PQM included the area under the curve (E_{AUC}, SAR_{AUC}, and CD_{AUC}), the 95% coverage or magnitude of fields encompassing 95% of a particular structure's volume ($E_{95\%}$, $SAR_{95\%}$, and $CD_{95\%}$), the median percent coverage or magnitude of fields encompassing 50% of a particular structure's volume ($E_{50\%}$, $SAR_{50\%}$, and $CD_{50\%}$), and hotspots defined by the 5% coverage or magnitude of fields encompassing 5% of a particular structure's volume ($E_{5\%}$, $SAR_{5\%}$, and $CD_{5\%}$).

Results

We found that TTFields could penetrate into the pelvic and abdominal cavities of the 2 patients (NS001 and BM002) for whom we performed finite element modeling (Fig 1). Both models shared certain commonalities but exhibited differences depending on the electric conductivities of various tissues. First, higher electric field intensities, as measured by the E_{AUC}, were observed mainly in bony structures such as the coccyx (880.4 and 266.2 V/m), ilium (374.6 and 343.3 V/m), ischium (445.8 and 197.7 V/m), and sacrum (282.4 and 342.8 V/m) of NS001 and BM002, respectively. In contrast, lower field intensities were found within tissues of the respective models such as the bladder (71.5 and 55.3 V/m) and colon (92.7 and 131.0 V/m) (Table 2). Although nonconductive gas in the colon was delineated, it is not considered as an anatomic structure and therefore it was not listed in the field metrics of tissues in Table 2. Second, higher energy deposition, as measured by SAR_{AUC}, was observed in the skin (14.7 and 30.1 W/kg) and bladder wall (14.7 and 10.0 W/kg), whereas the lowest was noted in the sacrum (1.5 W/kg) in NS001 and spinal cord (0.3 W/kg) in BM002. Lastly, the highest current density was identified in the bladder, CD_{AUC} 117.6 A/m^2 in NS001 and 89.5 A/m^2 in BM002, most likely due to the highly conductive intracavitary urine.

TTFields penetrate the CTVs within the pelvic and abdominal cavities

NS001 had malignant ascites, and therefore the CTV was essentially the peritoneal surface. The $E_{95\%}$ was 50.8 V/m, with a hotspot ($E_{5\%}$) of 161.3 V/m, wheres the $SAR_{95\%}$ was 2.4 W/kg with a hotspot ($SAR_{5\%}$) of 24.4 W/kg, and the corresponding $CD_{95\%}$ was 66.4 A/m^2 with a hotspot ($CD_{5\%}$) of 217.1 A/m^2. For the 2 CTVs in BM002, CTV_p is the primary ovarian carcinoma in the pelvic cavity and CTV_n is a lymph node metastasis in the abdominal cavity. For CTV_p, the $E_{95\%}$ was 79.4 V/m, with a hotspot ($E_{5\%}$) of 218.0 V/m, whereas the $SAR_{95\%}$ was 2.1 W/kg with a hotspot ($SAR_{5\%}$) of 15.3 W/kg; the $CD_{95\%}$ was 19.7 A/m^2 with a hotspot ($CD_{5\%}$) of 53.0 A/m^2. For CTV_n, the $E_{95\%}$ was 70.6 V/m, with a hotspot ($E_{5\%}$) of 153.0 V/m, whereas the $SAR_{95\%}$ was 1.5 W/kg with a hotspot ($SAR_{5\%}$) of 7.5 W/kg; the $CD_{95\%}$ was 15.4 A/m^2 with a hotspot ($CD_{5\%}$) of 38.5 A/m^2. Collectively, the parameters for AUC,

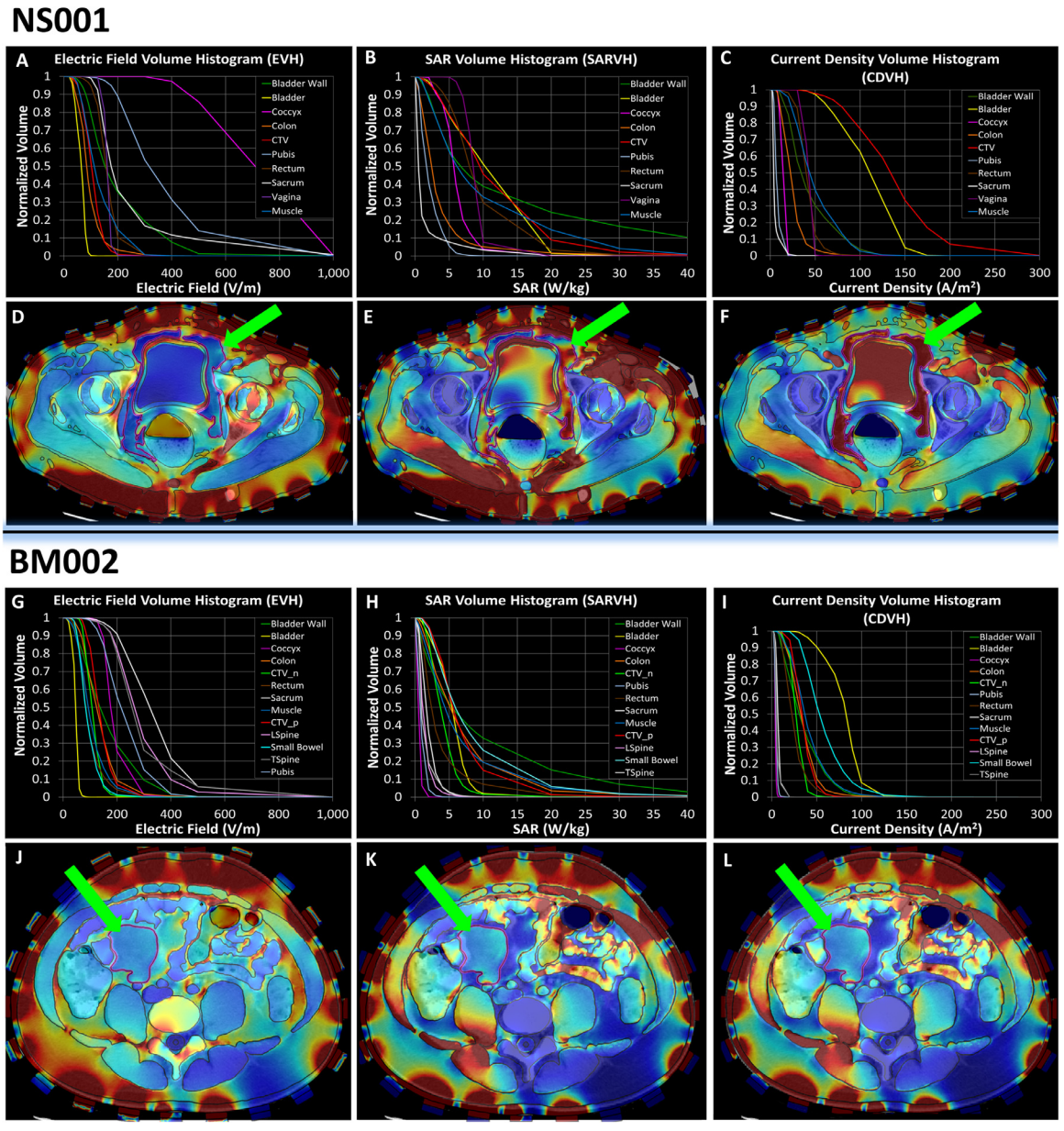

Figure 1 Electric field volume-histogram (EVH) (A), specific absorption rate volume-histogram (SARVH) (B), current density volume-histogram (CDVH) (C) of various segmented and evaluated structures in the pelvis of NS001 due to external application of Tumor Treating Fields (TTFields). Color wash overlay on computed tomography (CT) pelvic cross sections with clinical target volume (CTV) outlined in magenta (green arrow) of electric fields distribution (D), SAR distribution (E), and current density distribution (F). EVH (G), SARVH (H), CDVH (I) of various segmented and evaluated structures in the pelvis and abdomen of BM002 due to external application of TTFields. Color wash overlay on CT abdomen cross sections with CTV outlined in magenta (green arrow) of electric field distribution (J), SAR distribution (K), and current density distribution (L).

95%, 50%, and 5% of electric field, SAR, and current density were heterogeneous among the CTVs examined.

Sensitivity analysis of CTV electric conductivity on TTFields coverage

The tumor microenvironment is heterogeneous and the electric conductivity of different CTVs may vary. Therefore, we performed a sensitivity analysis on TTFields coverage by increasing the conductivity in log units from 0.001 to 100 S/m for each model. The overall field coverage progressively decreased as quantified by the E_{AUC}, $E_{95\%}$, $E_{50\%}$, and $E_{5\%}$ (Fig 2A-D). This result is consistent with the reduction in electric charge retention due to these charges moving through an increasingly conductive CTV at 200 kHz. This notion was corroborated by the inverted trend in the current density, as determined

Table 2 Plan quality metrics (PQM), derived from electric field volume histogram (EVH), specific absorption rate volume histogram (SARVH), current density volume histogram (CDVH), for each evaluated anatomical structure

Model	Tissue structure	E_{AUC}	$E_{95\%}$	$E_{50\%}$	$E_{5\%}$	SAR_{AUC}	$SAR_{95\%}$	$SAR_{50\%}$	$SAR_{5\%}$	CD_{AUC}	$CD_{95\%}$	$CD_{50\%}$	$CD_{5\%}$
NS001		**(V/m)**				**(W/kg)**				**(A/m^2)**			
	Anal Sphincter	250.7	132.6	160.2	190.9	17.4	9.0	13.3	18.4	92.7	52.3	62.4	75.5
	Bladder	71.5	31.9	64.6	85.7	10.1	2.4	10.2	18.1	117.6	55.4	111.8	149.6
	Bladder wall	212.4	66.2	152.1	432.7	14.7	1.3	6.7	54.4	47.9	14.1	33.7	96.1
	Cancellous bone	202.7	121.9	162.7	261.2	3.2	1.4	2.7	6.4	17.4	10.4	15.0	22.2
	Coccyx	880.4	430.0	684.0	918.0	6.9	2.6	5.7	9.6	18.9	8.7	13.9	18.5
	Colon	92.7	35.7	84.2	176.0	3.6	0.4	2.4	10.4	23.9	9.1	22.5	45.3
	CTV	112.9	50.8	101.5	161.3	10.9	2.4	9.5	24.4	145.1	66.4	134.1	217.1
	Gas	244.7	104.5	207.3	420.9	0.0	0.0	0.0	0.0	0.0	0.0	0.0	0.0
	Ilium	374.6	121.1	271.4	787.8	2.4	0.2	1.1	8.0	7.7	2.6	5.8	16.3
	Ischium	445.8	208.0	362.5	691.8	2.5	0.7	2.1	6.3	9.2	4.4	7.7	14.5
	Muscle	133.9	52.6	111.4	252.3	9.9	1.4	6.1	28.9	51.6	20.8	43.5	93.8
	Pubis	404.6	175.0	313.4	699.5	2.1	0.5	1.6	5.1	8.5	3.7	6.7	14.8
	Rectum	168.8	98.6	155.9	234.2	9.2	3.2	8.0	18.3	42.7	25.0	39.9	59.4
	Sacrum	282.4	118.6	174.8	691.6	1.5	0.1	0.5	7.9	5.6	2.4	3.8	14.5
	Skin	211.9	55.1	164.3	494.9	14.7	0.6	4.8	44.3	29.8	7.7	23.0	69.7
	Urethra	174.7	89.1	127.3	153.9	7.6	3.3	6.5	9.5	50.1	28.0	41.1	48.9
	Vagina	259.2	136.2	160.3	177.6	12.6	6.4	8.5	11.6	61.8	33.3	42.7	48.2
BM002	Anal Sphincter	77.5	45.7	56.9	69.0	1.7	1.1	1.6	2.6	32.5	15.2	24.1	28.7
	Bladder	55.3	24.4	46.6	59.6	5.3	1.4	5.4	8.6	89.5	42.5	83.0	107.2
	Bladder wall	166.9	40.7	137.2	345.1	10.0	0.5	5.4	34.3	38.2	9.0	30.5	76.5
	Bone	243.9	74.0	226.7	439.0	1.1	0.2	0.8	3.0	5.0	1.5	4.7	9.3
	Cancellous bone	172.0	43.8	161.8	327.1	3.7	0.2	2.6	11.1	14.5	3.6	13.7	27.7
	Coccyx	266.2	138.8	176.4	264.6	0.5	0.1	0.5	1.1	4.9	3.0	3.7	5.5
	Colon	131.0	58.9	124.1	236.8	7.0	1.2	5.1	17.7	33.9	14.3	32.0	58.1
	CSF	25.2	10.8	22.7	37.2	1.7	0.3	1.5	3.8	50.1	21.7	45.6	73.3
	CTV_n	139.0	70.6	106.9	153.0	4.1	1.5	3.7	7.5	36.3	15.4	26.8	38.5
	CTV_p	157.5	79.4	131.9	218.0	6.7	2.1	5.5	15.3	41.3	19.7	33.4	53.0
	Femur_LT	183.4	80.8	160.1	265.0	0.5	0.1	0.4	1.0	3.9	1.6	3.4	5.5
	Femur_RT	106.2	55.6	93.1	145.9	0.3	0.1	0.3	0.4	2.1	1.2	2.0	3.2
	Gallbladder	50.5	28.1	38.3	58.2	2.1	1.0	1.8	4.1	28.2	12.5	20.8	31.8
	Gas	267.1	87.0	236.5	491.8	0.0	0.0	0.0	0.0	0.0	0.0	0.0	0.0
	Ilium	343.3	133.0	284.8	652.8	1.8	0.2	1.3	5.4	7.2	2.8	6.1	13.8
	Ischium	197.7	99.4	169.2	292.9	0.6	0.1	0.4	1.4	4.3	2.1	3.5	6.3
	Kidney	169.0	72.0	129.7	236.4	5.4	1.4	4.2	13.6	33.2	13.4	26.3	44.4
	Liver	146.7	61.9	110.8	190.8	0.3	0.1	0.3	0.5	17.9	7.4	13.4	23.5
	Lspine	293.5	160.3	264.0	453.9	1.4	0.4	1.1	3.2	6.0	3.4	5.6	9.6

(*continued on next page*)

Table 2 (*Continued*)

Model	Tissue structure	E_{AUC}	$E_{95\%}$	$E_{50\%}$	$E_{5\%}$	SAR_{AUC}	$SAR_{95\%}$	$SAR_{50\%}$	$SAR_{5\%}$	CD_{AUC}	$CD_{95\%}$	$CD_{50\%}$	$CD_{5\%}$
	Muscle	107.5	35.7	93.2	204.2	6.8	0.6	4.3	20.6	41.3	13.2	36.5	79.2
	Pancreas	61.8	35.4	47.9	74.8	2.0	0.9	1.7	3.9	36.1	18.4	27.0	40.0
	Pubis	263.0	119.8	212.9	360.1	0.9	0.2	0.7	1.9	5.2	2.5	4.5	7.4
	Rectum	97.2	43.0	83.8	190.7	3.8	0.6	2.4	12.7	24.5	10.8	22.2	49.4
	Ribs	204.1	56.1	141.3	582.6	1.0	0.1	0.4	4.7	4.3	1.1	3.0	12.5
	Sacrum	342.8	173.2	321.6	534.2	1.9	0.5	1.6	4.1	7.1	3.7	6.8	12.2
	Skin	270.6	26.5	143.9	984.8	30.1	0.2	3.7	174.2	38.0	3.7	20.2	138.7
	Small bowel	101.4	48.1	83.4	159.0	8.3	2.0	5.9	21.6	63.9	30.6	53.0	101.0
	Spinal cord	36.4	14.7	28.2	42.2	0.3	0.1	0.3	0.4	3.3	1.5	2.8	4.1
	Spleen	81.3	41.1	60.5	84.9	0.7	0.2	0.7	1.3	11.4	5.5	8.1	13.2
	Stomach	52.4	33.1	49.8	68.5	1.9	0.8	1.7	3.3	28.1	16.9	26.4	37.7
	Tspine	299.2	162.7	254.5	549.1	1.5	0.4	1.0	4.3	6.1	3.4	5.3	12.0
	Uterus	78.0	42.9	69.8	93.7	3.5	1.2	3.3	6.0	42.4	22.8	36.9	50.4
	Vagina	111.0	59.0	69.4	86.8	2.2	1.1	1.6	2.6	27.1	11.6	16.3	25.6

Abbreviations: AUC = area under the curve; CD = current density; CDVH = current density volume histogram; CSF = cerebrospinal fluid; CTV = clinical target volume; CTV_n = CTV for lymph node metastasis in the abdominal cavity; CTV_p = CTV for primary ovarian carcinoma in the pelvic cavity; E = electric field; EVH = electric field volume histogram; LT = left; PQM = Plan quality metrics; RT = right; SAR = specific absorption rate; SARVH = specific absorption rate volume histogram.

by the CD_{AUC}, $CD_{95\%}$, $CD_{50\%}$, and $CD_{5\%}$, where a higher CTV conductivity resulted in higher current density (Fig 2I-L). The behavior of these curves likely indicates that the field intensity will plateau when the conductivity of the CTVs reaches anatomically and clinically irrelevant limits. In contrast, when plotting the SAR_{AUC}, $SAR_{95\%}$, $SAR_{50\%}$, and $SAR_{5\%}$ as a function of electric conductivity, a characteristic maximum SAR was observed in each plot, indicating that there is a peak conductivity for the individual CTVs to receive maximum power absorption at 200 kHz (Fig 2E-H).

Array disposition alters the distribution of TTFields in the CTV

Although the patient's anatomy and tumor are fixed, the delivery of TTFields can be adjusted on the skin surface. We next asked whether or not TTFields can be maximally distributed to the CTV by altering the positioning of the arrays. For this purpose, the arrays were rotated between 0˚ and 75˚ in a clockwise fashion (Fig 3). The axis of rotation was defined along the longitudinal length of the body. Of note, due to the geometric symmetry of the array setup, this analysis did not require further rotation at 90˚ or beyond. For the CTV in NS001 and CTV_p in BM002, array disposition did not affect electric field coverage as defined by E_{AUC}, $E_{95\%}$, or $E_{5\%}$ (Fig 4A-D). However, CTV_n in BM002 had the highest field strength when the arrays were rotated near 50˚, with an increase in E_{AUC} of 79.1%, $E_{95\%}$ of 77.3%, and $E_{5\%}$ of 78.8% compared with the original position at 0˚ (Fig 3A-D). Similarly, a 50˚ rotation for CTV_n in BM002 maximized the respective SAR_{AUC}, $SAR_{95\%}$, and $SAR_{5\%}$ to 216.3%, 234.7%, and 191.66% (Fig 4E-H), as well as the respective CD_{AUC}, $CD_{95\%}$, and $CD_{5\%}$ to 55.6%, 107.1%, and 67.6% (Fig 4I-L). Collectively, our data indicate that optimum TTFields coverage of the CTV, as quantified by the metrics of E, SAR, and CD, are unique to the positioning of the CTVs relative to the patient's anatomy.

Variability of TTFields within the bladder

Because the bladder often contains urine and the composition of urine consists of highly conductive electrolytes, it is expected that the electric field strength within the bladder would be reduced. Indeed, bladder has lower electric field strength compared with other tissues (Table 2), and therefore its fluid content and positioning may alter TTFields coverage of the CTV. When the electric conductivity of the bladder was altered, large changes in the field strength within the bladder were observed in the NS001 model, whereas changes in BM002 were modest (Fig E1). Similar changes were also noted in the SAR and CD in both models. Interestingly, when using any of

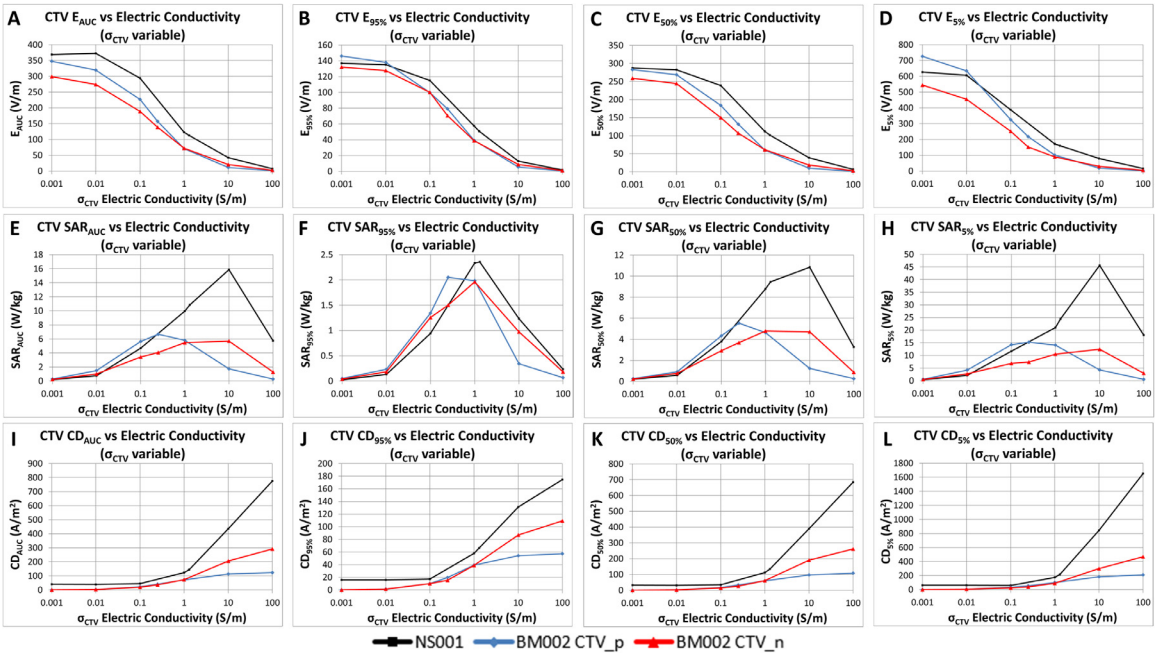

Figure 2 Sensitivity analysis of clinical target volume (CTV) electric conductivity on electric field, specific absorption rate (SAR), and current density plan quality metrics (PQM). As electric conductivity increased from 0.001 to 100 S/m, the electric field strength decreased within the CTV in terms of its electric field area under the curve (E_{AUC}), 95% coverage ($E_{95\%}$), median coverage ($E_{50\%}$), and $E_{5\%}$ hotspot (A-D). In contrast, there was an inverted parabolic behavior in SAR (E-H). There was an increase in the current density as a function of electric conductivity (I-L).

the 3 metrics used to quantify field strength within the bladder, a maximum value was observed when the electric conductivity of the bladder was set at 1 S/m in the BM002 model, whereas a maximum was seen only in the SAR metrics for NS001 (Fig E1). These differences might be related to the deformed and nondeformed shapes of the respective bladders in the BM002 and NS001 models (Fig E2). The deformation of the bladder in BM002 was due to the presence and location of the patient's very large CTV_p encroaching on the space in which bladder is normally situated. Regardless, TTFields at the CTV was largely unaffected by changes in the electric conductivity of the bladder up to 1 S/m (Fig E3).

Discussion

According to International Commission on Radiological Units and Measurements Report 62, updated recommendations on dose-volume reporting were established for radiation oncology treatment planning[6]. Dose-volume metrics such as the $D_{95\%}$ and $D_{50\%}$ were recommended to be reported as they were considered to be good measures of typical dose in a relatively homogenous treatment plan at the target(s). Other PQMs were also recommended to be reported along with all treatment plans as a means to evaluate the quality of the treatment plan and how well it meets prescription objectives and constraints in both normal tissues and target(s). In this study, we make use of similar PQM metrics, such as (1) $E_{95\%}$, $SAR_{95\%}$, and $CD_{95\%}$; (2) $E_{50\%}$, $SAR_{50\%}$, and $CD_{50\%}$; as well as (3) $E_{5\%}$, $SAR_{5\%}$, and $CD_{5\%}$, to compare the field coverage between models. This is because there is currently no known established standard definition of prescribed dose to be delivered by TTFields at the targets. We have shown that TTFields can penetrate from the skin surface into the pelvic and abdominal cavities to achieve coverage of the CTV. Varying the electric conductivity and array positioning can profoundly alter the field distributions. Although bladder conductivity and shape also played some role in affecting TTFields coverage to the CTV, the results were generally minor. The exact contribution from the electrolyte composition of the bladder fluid is unclear.

TTFields exhibit a characteristic SAR maximum

We used SAR as a means of quantifying the rate of energy delivered to the CTV. Compared with the Gray measurement in joules/kilogram currently used for ionizing radiation, SAR in watts/kilogram or joules/s/kilogram is better suited to measure energy delivery from continuous treatment using TTFields, whereas the electric field in volt/meter primarily associates with the depth of penetration[1,12,28]. It is notable that the peak on each of the SAR plots as a function of electric conductivity (as shown in Fig 2E-H) indicates distinctly a maximum

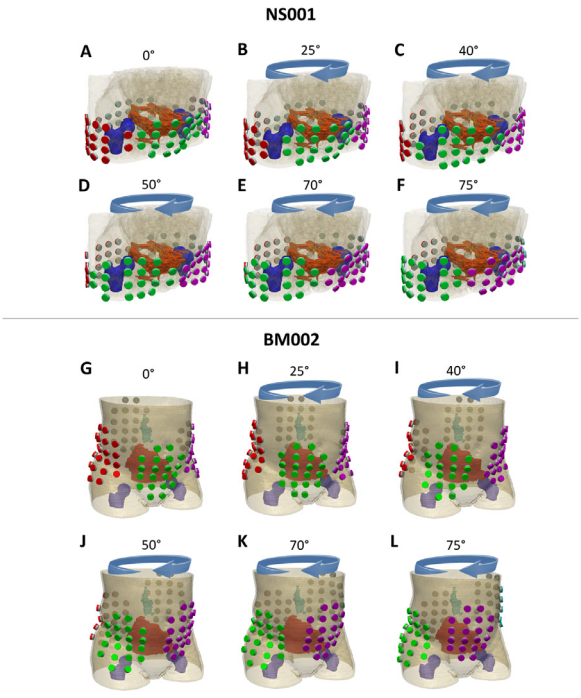

Figure 3 Array rotation configurations for NS001 (A-F) and BM002 (G-L). The green arrays represent the anteroposterior (AP) arrays, the cyan arrays represent the posteroanterior (PA) arrays, the red arrays represent the right lateral (RLAT) arrays, and the purple arrays represent the left lateral (LLAT) arrays. Array placement is shown without any clockwise rotation (A and G), 25° clockwise rotation (B and H), 40° clockwise rotation (C and I), 50° clockwise rotation (D and J), 70° clockwise rotation (E and K), and 75° clockwise rotation (F and L).

power absorption in the CTV based on the conditions that were modeled. A similar investigation was performed in the brain model of a patient with a right parietal glioblastoma[10]. In that study, the mean SAR of the GTV did not result in an inverted parabola but rather a sigmoidal function. These differences in the behavior of the SAR plots suggest that SAR within the GTV or CTV probably comprise a delicate balance between the volume/physical density of the target and the electric field intensity within the patient's anatomy when TTFields is applied. In addition, it should be noted that our ovarian cancer CTVs were located centrally within the abdomen and pelvis, whereas the glioblastoma GTV in the other study was lateralized to the right cerebral hemisphere[10]. Because SAR often decays exponentially within tissues from near-field sources, we speculate that there exists a relationship not only involving tissue conductivity but also depth from the 2 pairs of abdominal arrays (Fig 2E-H)[9,19]. However, the asymmetry of the glioblastoma within the head might alter the SAR plot as a function of conductivity. Furthermore, CTV_n had the highest SAR peak compared with that from CTV_p from BM002 and CTV from NS001. This is probably due to the inverse relationship between SAR and volume of the target, where a smaller target volume would have a higher SAR compared with a larger target volume for a given amount of applied electric fields. Therefore, the location of the ovarian cancer target and the patient's anatomy influence the delivery of TTFields.

The electric conductivity of the CTVs in NS001 and BM002 is different, as seen in Table 1. The CTV in NS001 is representative of fluid composition because there is no solid tumor present. On the contrary, both CTVs in BM002 represent solid tumor masses that are Fluorodeoxyglucose avid on PET. When the CTVs were assigned with very low conductivity or high impedance values, the SAR metrics approached zero (Fig 2E-H). This would be analogous to a scenario where there is little to no change in electric potential in this region, resulting in little to no energy absorbed by the tissue, that is, no work done and therefore no power absorbed by the mass of medium. A different effect with similar SAR intensity is also observed when the electric conductivity of the CTV is extremely high, where the SAR is very low, along with a low electric field intensity due to nearly no charge retention within the structure at 200 kHz. Therefore, these differences in conductivity might play a distinctive role in modulating the field intensities within these volumes, indicating that choice of electric properties applied when modeling CTV(s) will also alter predictions of field distributions.

TTFields coverage of the CTV can be maximized by array rotation

When the arrays were rotated, we found similar results in BM002, but not NS001, to those reported by Korshoej et al[8], where the maximum effect in field delivery to the tumor was found when the arrays were rotated with an approximately 45° offset from central axis at midline. One major difference between their study and this one is that their tumor was located very lateral while the CTVs in our study were situated quite centrally. One important observation noted by rotating the arrays is that the rotation from central axis at midline actually degraded the coverage to the CTV for NS001 but yielded a maximum effect near 50° for both the CTV_p and CTV_n in BM002. The latter effect is likely similar to that described by Korshoej et al[8]. These results suggest that array positioning can potentially optimize electric field delivery to the intended target.

TTFields are distributed differently within the pelvic and abdominal cavities

Our modeling shows that, in general, cortical bone structures receive higher electric field intensity than soft

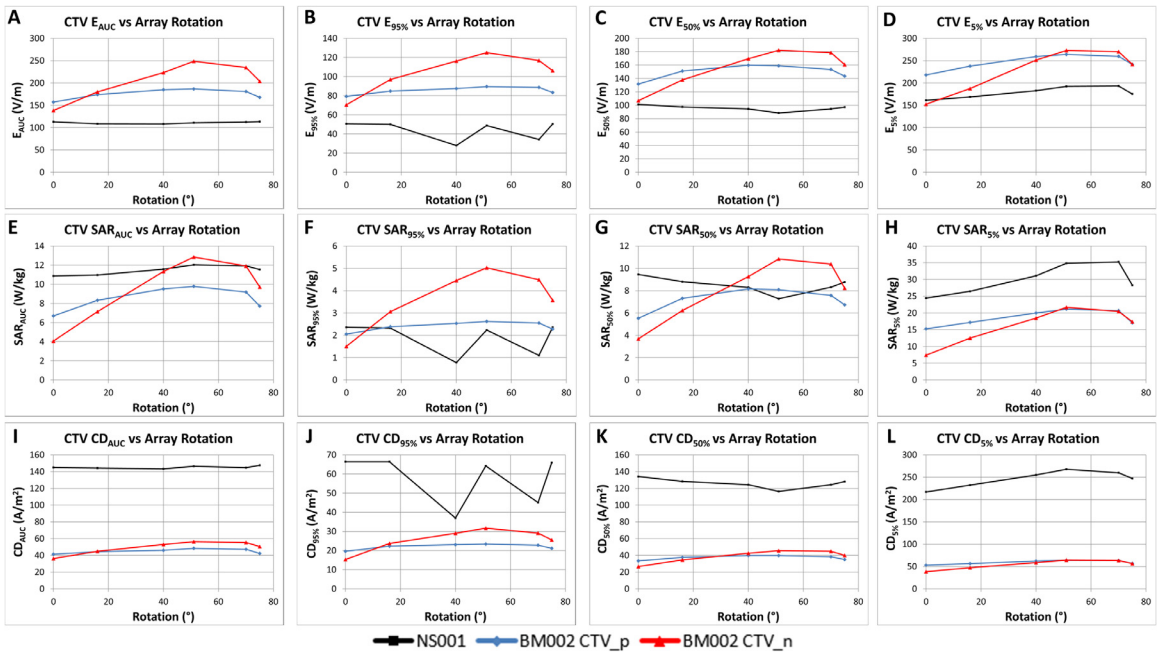

Figure 4 Analysis of array rotation on clinical target volume (CTV) coverage evaluated by electric field, specific absorption rate (SAR), and current density. There was no significant difference in the plan quality metrics (PQM) when the arrays were rotated clockwise between 0 and 75° for electric field (A-D), SAR (E-H), and current density (I-L) for NS001 and the CTV for primary ovarian carcinoma in the pelvic cavity (CTV_p) for BM002. However, there were larger variations in coverage to the CTV for lymph node metastasis in the abdominal cavity (CTV_n) of BM002 as a function of array rotation, with a peak at 50°.

tissues. This is because higher impedance materials like cortical bone will have a higher rate of charge retention, thereby increasing electric field intensity in these regions. In contrast, the bladder usually contains electrically conductive urine, while the spinal cord is surrounded by a column of highly conductive cerebrospinal fluid. Therefore, current density flowing through these regions is expected to be much higher compared with the lower conductive soft tissues such as the liver, bladder wall, and cancellous bone. By applying TTFields externally at 200 kHz, there is unlikely enough time for charge retention within the bladder to occur, therefore decreasing the overall electric field strength.

Skin in both models had the highest SAR_{AUC}, and this is most likely due to the proximity of the electrode/gel-skin interface at the body surface, allowing greatest exposure to TTFields. Interestingly, colon in NS001 was ranked one of the lowest in electric field strength, while this was not the case in BM002. This disparity might be due to the differences in volume of colonic gases and fecal matter present between the models, where gas is nonconductive, thereby reducing the current density distribution in this region and forcing the electric field intensity to decrease. It should be noted that because gas mixture within the digestive tract and fecal volume can be highly variable, the results from this study alone should not be used to generalize the effects they have on TTFields.

One of the crucial differences between the NS001 and BM002 models is that the array placements are slightly different. Because of the larger circumference of the pelvis, the arrays on NS001 can be positioned horizontally, whereas on BM002 the arrays had to be placed vertically. Additionally, due to the extent of the disease in BM002, extending from the middle of the pelvis rostrally to the middle of the abdomen, a slight modification of the array placement was necessary to provide sufficient coverage to both CTV_p and CTV_n. This is done by (1) repositioning the anteroposterior array inferiorly, (2) shifting the posteroanterior array superiorly, and (3) centering both lateral arrays midlevel between both CTVs. The variability in TTFields between both models suggests that electric field distribution is not only sensitive to changes in material properties and array placements, but also to anatomic differences within the pelvis and abdomen. Our results demonstrate the utility of personalized modeling that can enable clinicians to better optimize the delivery of TTFields for patients with ovarian cancer.

Conclusions

To our knowledge, this is the first comprehensive modeling study of TTFields for ovarian cancer and we showed that these fields can penetrate the pelvis and abdomen. The use of PQM enabled us to quantify and

evaluate the extent of coverage to the CTVs and normal tissues. Field strength quantified by these metrics revealed a heterogeneous distribution of field intensity throughout the pelvis and abdomen. Altering the conductivity of the CTVs resulted in varying field coverage within the target, whereas rotating the arrays may reveal significant changes in CTV coverage. Future phantom measurements are required to validate the results of our in silico modeling of TTFields.

Supplementary materials

Supplementary material associated with this article can be found in the online version at https://doi.org/10.1016/j.adro.2021.100716.

References

1. Ballo MT, Urman N, Lavy-Shahaf G, Grewal J, Bomzon Z, Toms S. Correlation of tumor treating fields dosimetry to survival outcomes in newly diagnosed glioblastoma: a large-scale numerical simulation-based analysis of data from the phase 3 EF-14 randomized trial. *Int J Radiat Oncol Biol Phys*. 2019;104:1106–1113.
2. Burger RA, Brady MF, Bookman MA. Incorporation of bevacizumab in the primary treatment of ovarian cancer. *New Engl J Med*. 2011;365:2473–2483.
3. Ceelen WP, Flessner MF. Intraperitoneal therapy for peritoneal tumors: Biophysics and clinical evidence. *Nat Rev Clin Oncol*. 2009;7:108–115.
4. Giladi M, Schneiderman RS, Voloshin T, et al. Mitotic spindle disruption by alternating electric fields leads to improper chromosome segregation and mitotic catastrophe in cancer cells. *Sci Rep*. 2015;5:18046.
5. Gonzalez-Martin A, Pothuri B, Vergote I. Niraparib in patients with newly diagnosed advanced ovarian cancer. *New Engl J Med*. 2019;381:2391–2402.
6. International Commission on Radiation Units and Measurements. Prescribing, recording and reporting photon beam therapy (supplement to ICRU Report 50). *J ICRU*. 1999.
7. Kaufman B, Shapira-Frommer R, Schmutzler RK, et al. Olaparib monotherapy in patients with advanced cancer and a germline BRCA1/2 mutation. *J Clin Oncol*. 2015;33:244–250.
8. Korshoej AR, Hansen FL, Mikic N, von Oettingen G, Sorensen JCH, Thielscher A. Importance of electrode position for the distribution of tumor treating fields (TTFields) in a human brain. Identification of effective layouts through systematic analysis of array positions for multiple tumor locations. *PLoS One*. 2018;13: e0201957.
9. Liorni I, My Capstick, van Wel L, et al. Evaluation of specific absorption rate in the far-field, near-to-far field and near-field regions for integrative radiofrequency exposure assessment. *Radiat Protect Dosimet*. 2020;190:459–472.
10. Lok E, San P, Hua V, Phung M, Wong ET. Analysis of physical characteristics of Tumor Treating Fields for human glioblastoma. *Cancer Med*. 2017;6:1286–1300.
11. Matulonis UA, Sood AK, Fallowfields L, Howitt BE, Sehouli J, Karlan BY. Ovarian cancer. *Nat Rev Dis Primer*. 2016;2:16061.
12. Miranda PC, Mekonnen A, Salvador R, Basser PJ. Predicting the electric field distribution in the brain for the treatment of glioblastoma. *Phys Med Biol*. 2014;59:4137–4147.
13. Moore K, Colombo N, Scambia G. Maintenance olaparib in patients with newly diagnosed advanced ovarian cancer. *New Engl J Med*. 2018;379:2495–2505.
14. Moore KN, Secord AA, Geller MA, et al. Niraparib monotherapy for late-line treatment of ovarian cancer (QUADRA): A multicentre, open-label, single-arm, phase 2 trial. *Lancet Oncol*. 2019;20:636–648.
15. Ozols RF, Bundy BN, Greer BE, et al. Phase III trial of carboplatin and paclitaxel compared with cisplatin and paclitaxel in patients with optimally resected stage III ovarian cancer: A Gynecologic Oncology Group study. *J Clin Oncol*. 2003;21:3194–3200.
16. Penson RT, Valencia RV, Cibula D, et al. Olaparib versus nonplatinum chemotherapy in patients with platinum-sensitive relapsed ovarian cancer and a germline BRCA1/2 Mutation (SOLO3): A randomized phase III trial. *J Clin Oncol*. 2020;38:1164–1174.
17. Pujade-Lauraine E, Hilpert F, Weber B, et al. Bevacizumab combined with chemotherapy for platinum-resistant recurrent ovarian cancer: The AURELIA open-label randomized phase III trial. *J Clin Oncol*. 2014;32:1302–1308.
18. Salmanzadeh A, Sano MB, Gallo-Villanueva RC, Roberts PC, Schmelz EM, Davalos RV. Investigating dielectric properties of different stage of syngeneic murine ovarian cancer cells. *Biomicrofluidics*. 2013;7:1058–1932.
19. Stuchly SS, Stuchly MA, Kraszewski A, Hartsgrove G. Energy deposition in a model of man in the near field. *Bioelectromagnetics*. 1985;6:115–129.
20. Stupp R, Taillibert S, Kanner A, et al. Effect of tumor-treating fields plus maintenance temozolomide vs maintenance temozolomide alone on survival in patients with glioblastoma. *JAMA*. 2017;318:2306–2316.
21. Stupp R, Wong ET, Kanner AA, et al. NovoTTF-100A versus physician's choice chemotherapy in recurrent glioblastoma: A randomised phase III trial of a novel treatment modality. *EJC*. 2012;48:2192–2202.
22. Swisher EM, Lin KK, Oza AM, et al. Rucaparib in relapsed, platinum-sensitive high-grade ovarian carcinoma (ARIEL2 Part 1): An international, multicentre, open-label, phase 2 trial. *Lancet Oncol*. 2017;18:75–87.
23. van Baal JOAM, van Noorden CJF, Nieuwland R, et al. Development of peritoneal carcinomatosis in epithelial ovarian cancer: A review. *J Histochem Cytochem*. 2018;66:67–83.
24. Vergote I, von Moos R, Manso L, Nieuwenhuysen EV, Concin N, Sessa C. Tumor Treating Fields in combination with paclitaxel in recurrent ovarian carcinoma: Results of the INNOVATE pilot study. *Gynecol Oncol*. 2018;150:471–477.
25. Voloshin T, Munster M, Blatt R, et al. Alternating electric fields (TTFields) in combination with paclitaxel are therapeutically effective against ovarian cancer cells in vitro and in vivo. *Int J Cancer*. 2016;139:2850–2858.
26. Wegner C, Salvador R, Basser PJ, Miranda PC. Improving tumor treating fields treatment efficacy in patients with glioblastoma using personalized array layouts. *Int J Radiat Oncol Biol Phys*. 2016;94:1137–1143.
27. Wenger C, Miranda PC, Salvador RN, Basser PJ. Alternating electric fields (TTFields) for treating glioblastomas: A modeling study on efficacy. *Neuro-Oncol*. 2014:16.
28. Wenger C, Salvador R, Basser PJ, Miranda PC. The electric field distribution in the brain during TTFields therapy and its dependence on tissue dielectric properties and anatomy: A computational study. *Phys Med Biol*. 2015;60:7339.
29. Mulhall H, Labeed F, Kazmi B, Costea D, Hughes M, Lewis M. Cancer, pre-cancer and normal oral cells distinguished by dielectrophoresis. *Analytical and Bioanalytical Chemistry*. 2011;401:2455–2463.